

Plasma Parameters and the Reduction Potential at a Plasma-Liquid Interface

[Electronic Supplementary Information]

Trey Oldham¹, Shurik Yatom², and Elijah Thimsen^{1,3,a)}

¹ Department of Energy, Environmental & Chemical Engineering, Washington University in St. Louis, St. Louis, MO, USA

² Princeton Plasma Physics Laboratory, Princeton University, Princeton, NJ, USA

³ Institute of Materials Science & Engineering, Washington University in St. Louis, St. Louis, MO, USA

^{a)} **Author to whom correspondence should be addressed:** elijah.thimsen@wustl.edu

Supplementary Note 1: Laser Heating

Laser heating of electrons in plasmas are known to occur as a result of inverse bremsstrahlung, where photons are absorbed by the plasma.^{1,2} The threshold value for the laser fluence able to increase the electron temperature due to the absorption of energy from the incident laser has been worked out by Carbone et al.³ in the case of a nonthermal argon (Ar) plasma. The critical value of the ionization degree for an argon plasma is given by

$$\alpha_{crit} = 3.4 \cdot 10^{-5} (k_B T_e)^{3/2} [1 + 6.4 \cdot (k_B T_e) + 14.2 \cdot (k_B T_e)^2] \quad (S1)$$

where k_B is the Boltzmann constant and T_e is the electron temperature. The rate coefficient for momentum transfer from electrons to ions is written as

$$K_{ei} = 2.54 \cdot 10^{-11} \left(\frac{1}{k_B T_e} \right)^{3/2}. \quad (S2)$$

The number density of atoms is expressed as

$$n_a = \frac{p}{k_B T_h} - n_e \quad (S3)$$

where p is the pressure, T_h is the temperature of heavy particles, and n_e is the electron density. The maximum allowable relative increase in electron temperature is set by the experimentalist and can be written as

$$\xi = \frac{\Delta(k_B T_e)}{k_B T_e}. \quad (S4)$$

Assuming quasi-neutrality ($n_e = n_i$), the critical laser fluence can be expressed as³

$$F_{crit} = 24 \pi^4 \frac{m_e \epsilon_0 c^3}{q_e^2} \cdot \frac{1}{\lambda_0} \cdot \xi \cdot \frac{k_B T_e}{n_e K_{ei}} \left[1 + \frac{n_a}{n_e} \alpha_{crit} \right]^{-1} \quad (S5)$$

where m_e is the rest mass of an electron, ϵ_0 is the permittivity of free space, c is the speed of light in a vacuum, q_e is the fundamental charge, and λ_0 is the central laser wavelength. For $k_B T_e = 1.0$ eV, $n_e = 1.0 \cdot 10^{22}$ m⁻³, and $\xi = 0.05$ the critical laser fluence was determined to be $F_{crit} = 135.1$ J cm⁻², which was greater than the operating laser fluence used in the experiments $F_{exp} = 75.6$ J cm⁻².

In addition to the theoretical calculation for the critical laser fluence for laser heating of electrons, the experimental values of $k_B T_e$ were obtained from Thomson scattering measurements over a range of laser fluences. Examples of the Thomson signal acquired for the radiofrequency (RF) Ar atmospheric pressure plasma jet (APPJ) operating at 50 W using a laser fluences of 44.1 J cm⁻² (pulse energy of 35 mJ) and 226.6 J cm⁻² (pulse energy of 180 mJ) are shown in Figs. S1a and S1b, respectively. The laser spot size was 318 μ m in diameter and the laser pulse energy was adjusted 35 to 180 mJ per pulse. A plot of the measured $k_B T_e$ as function of laser fluence is shown in Fig. S1c. The laser fluence (F_{exp}) used in the experiments is indicated by the dashed blue line. The operating laser fluence used in the Thomson and Raman scattering experiments was within the range in which the mean value of $k_B T_e$ remained constant. Above the theoretical laser fluence (F_{crit}), the electron temperature begins to increase.

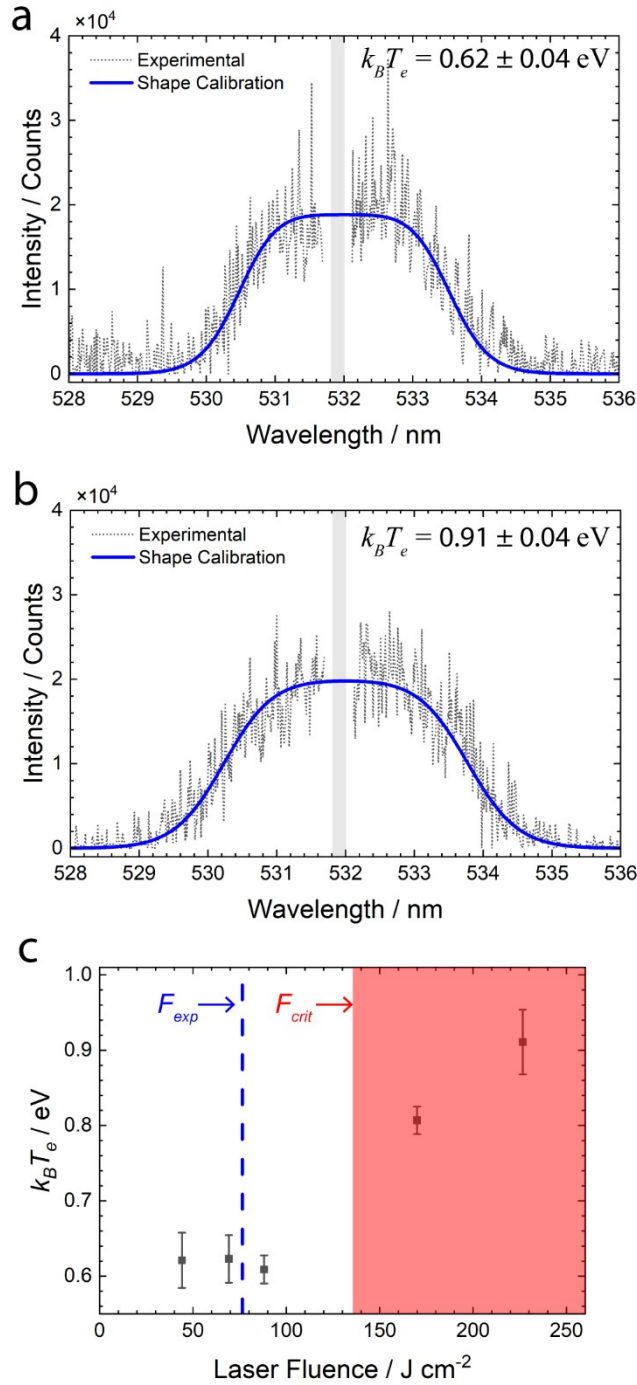


Fig. S1. Electron temperature as a function of laser fluence. Thomson signal acquired for Ar plasma generated using an applied RF power of 50 W using a laser fluence of (a) 44.1 J cm^{-2} (laser pulse energy of 35 mJ) and (b) 226.6 J cm^{-2} (laser pulse energy of 180 mJ). The grayed out region is the Rayleigh rejection region. (c) The measured values of $k_B T_e$ as a function of laser fluence. Blue dashed line indicates the laser fluence used in the Thomson and Raman scattering experiments (F_{exp}) and shaded red area indicates the laser fluences at or above the critical value (F_{crit}) required for electron heating.

Supplementary Note 2: iCCD Images of Raman and Thomson Scattering

Examples of the raw images acquired by the intensified CCD (iCCD) camera in the Raman and Thomson scattering experiments are shown in Fig. S2. The images were accumulated over 10000 laser shots (17 min). The Rayleigh rejection region is grayed out about the central wavelength of $\lambda_0 = 532$ nm. In both images, the vertical axis indicates the axial position along the direction of the laser beam, while the horizontal axis shows the spectral dispersion (wavelength). The experimental Raman spectrum shown in Fig. 3a of the main text was generated by summing the pixels in Fig. S2a along the vertical direction. Similarly, the experimental Thomson spectra acquired for the Ar APPJ operating at 50 W shown in Figs. 3b and 3c were generated by summing the pixels in Fig. S2b along the vertical direction.

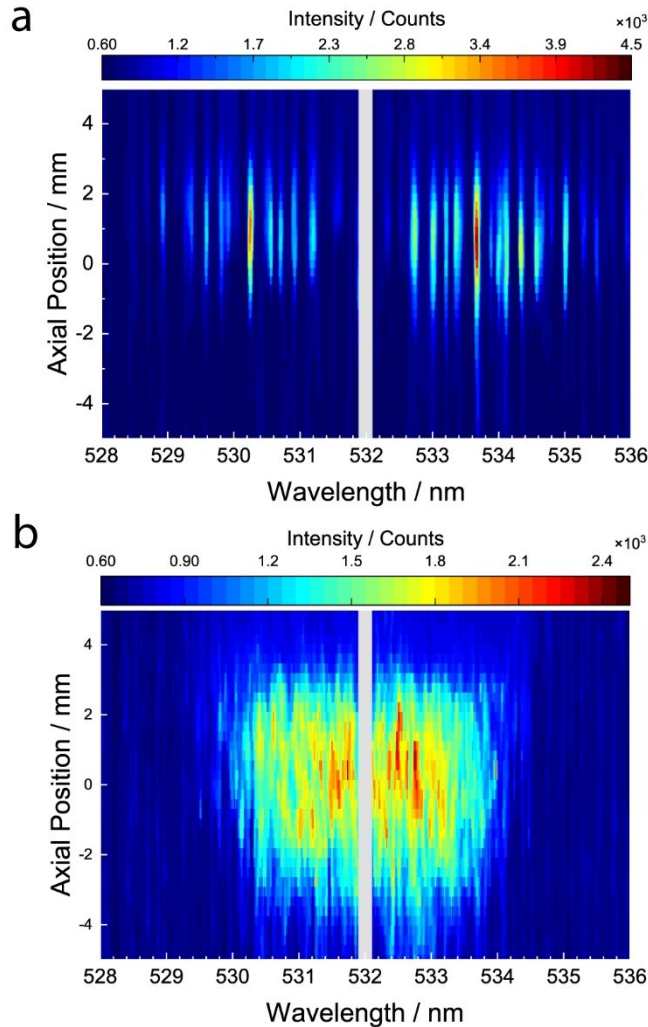


Fig. S2. Raw iCCD images for Raman and Thomson scattering. (a) The iCCD image acquired for Raman scattering in open air under ambient conditions with no discharge present. (b) The iCCD image acquired for Thomson scattering of Ar APPJ operating at 50 W. Both images were accumulated over 10000 laser shots (17 min) using a laser pulse energy of 60 mJ.

Supplementary Note 3: Ultraviolet-Visible Absorption Spectroscopy

Plasma treatments of indigo carmine (IC) were performed with the same (13.56 MHz) Ar APPJ used in the Thomson scattering experiments to verify the selective reduction of the redox indicator. The APPJ was comprised of a powered nickel needle electrode with an outer diameter of 2.3 mm housed within a dielectric tube with inner and outer diameters of 3.2 mm and 9.5 mm, respectively. The ground electrode was an aluminum ring with an inner diameter of 9.5 mm, which was mounted to the exterior of the dielectric tube 5 mm from the tube outlet. The Ar flow rate was maintained at a constant flow rate of 1000 standard cubic centimeters per minute (sccm) using a mass flow controller (GE50A, MKS Instruments). The plasma was generated using a RF power supply (AG 0613, T&C Power Conversion) connected to an impedance matching network (AIT-600 RF Auto Tuner, T&C Power Conversion). A function generator (4053B Arbitrary Waveform Generator, BK Precision) was used to modulate the RF excitation frequency with a 20 kHz square wave pulse with a duty cycle of 20%.

A fresh IC solution was prepared with a nominal concentration of 75 μM and an adjusted pH of 10. Plasma treatments were performed using a gap height of 10 mm between the end of the APPJ tube and the solution surface. Treatments were performed on 20 mL volumes for a duration of 60 s using the same applied RF powers used in the Thomson scattering experiments. Immediately following treatment, 2 mL aliquots were drawn and used for ultraviolet-visible (UV-Vis) absorption spectroscopy. The UV-Vis absorption spectra were acquired on a Cary 5000 spectrophotometer (Agilent) over the wavelength range of 350-700 nm using a scan rate of 150 nm min^{-1} . The UV-Vis absorption spectra for IC solutions treated at various RF powers are shown in Fig. S3. The presence of the isosbestic points in the IC absorption spectrum, indicated in Fig. S3b, revealed that the Ar APPJ used in this work was able to selectively reduce the redox indicator without forming degradation byproducts.⁴

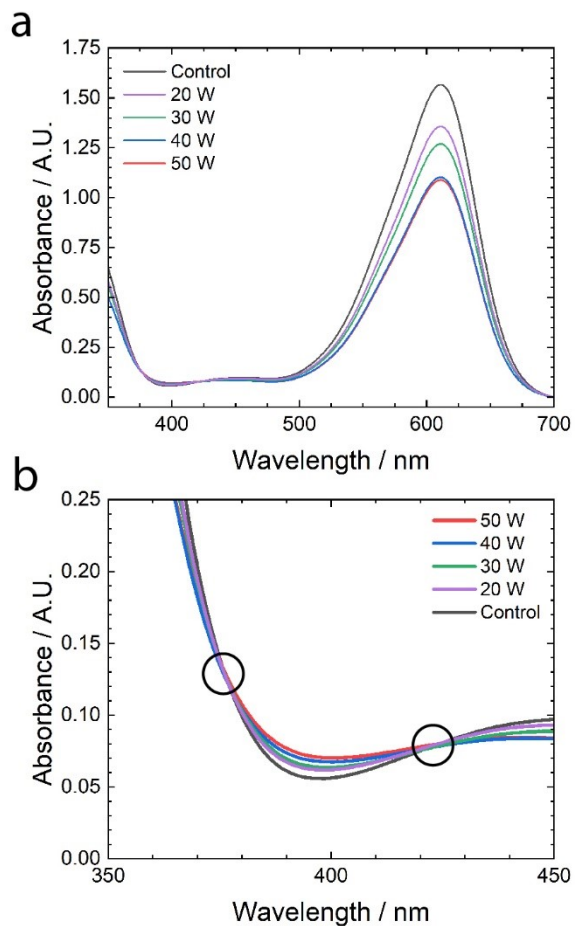


Fig. S3. Ultraviolet-Visible Absorption Spectrum of Indigo Carmine. (a) UV-Vis absorption spectra of plasma treated IC solutions with an initial concentration of $75 \mu\text{M}$ and pH of 10 as a function of applied RF power. Plasma treatments were performed on 20 mL treatment volumes for a duration of 60 s. (b) Zoomed-in portion of absorption spectra shown in (a) to illustrate that the isosbestic points were preserved following plasma treatments using the Ar APPJ.

Supplementary Note 4: Effect of Scattering Parameter on Spectral Distribution Function

The degree of collectivity is determined by the scattering parameter α , given by

$$\alpha = \frac{1}{2\sqrt{2}\pi} \cdot \frac{\lambda_0}{\lambda_D} \quad (\text{S6})$$

where λ_D is the electron Debye length of the plasma expressed as

$$\lambda_D = \left(\frac{\varepsilon_0 k_B T_e}{q_e^2 n_e} \right)^{1/2}. \quad (\text{S7})$$

Note that the first term on the righthand side of Equation S6 only applies to light scattering systems in which the detection axis is orthogonal to the incident laser. In the collective Thomson scattering regime (*i.e.* $\lambda_0 \gg \lambda_D$), the incident laser light is scattered by an ensemble of electrons, resulting in anisotropic scattering of light. Due to the non-uniform scattering of light, interference effects distort the pure Gaussian profile of the spectral distribution function. The modification of the spectral distribution function can be written in terms of the scattering parameter α as

$$S_e(x_e) = \frac{1}{\sqrt{\pi}} \cdot \frac{\exp(-x_e^2)}{|1 + \alpha^2 W(x_e)|^2} \quad (\text{S8})$$

where x_e is a dimensionless parameter and $W(x_e)$ is the plasma dispersion function. The value of x_e is given by

$$x_e = \frac{c\lambda_0}{\sqrt{2}} \cdot \left(\frac{1}{\lambda} - \frac{1}{\lambda_0} \right) \cdot \left(\frac{2k_B T_e}{m_e} \right)^{-1/2}. \quad (\text{S9})$$

The complex plasma dispersion is expressed as

$$W(x_e) = 1 - 2x_e e^{-x_e^2} \int_0^{x_e} e^{t^2} dt - j\sqrt{\pi} x_e e^{-x_e^2} \quad (\text{S10})$$

where t is a dummy variable and j is an imaginary unit. The principle of the shape calibration approach is illustrated in Fig. S4. First, the α is used to adjust the shape of the spectral distribution function calculated using Equation S8 until it resembles the shape of the experimental Thomson signal. The influence of α on the shape of the spectral distribution function is shown in Fig. S4a. Next, the width of S_e is adjusted by holding α constant and varying $k_B T_e$, until a suitable fit with the experimental Thomson spectrum is obtained. The influence of $k_B T_e$ on the width of the spectral distribution function, for constant α ($\alpha = 0.8$), is shown in Fig. S4b. Once the unique values of α and $k_B T_e$ that accurately fit the Thomson signal are determined, the corresponding value of n_e is back-calculated by combining and rearranging Equations S6-7, yielding

$$n_e = \frac{\varepsilon_0 k_B T_e}{q_e^2} \left(\frac{1}{2\sqrt{2}\pi} \cdot \frac{\lambda_0}{\alpha} \right)^{-2}. \quad (\text{S11})$$

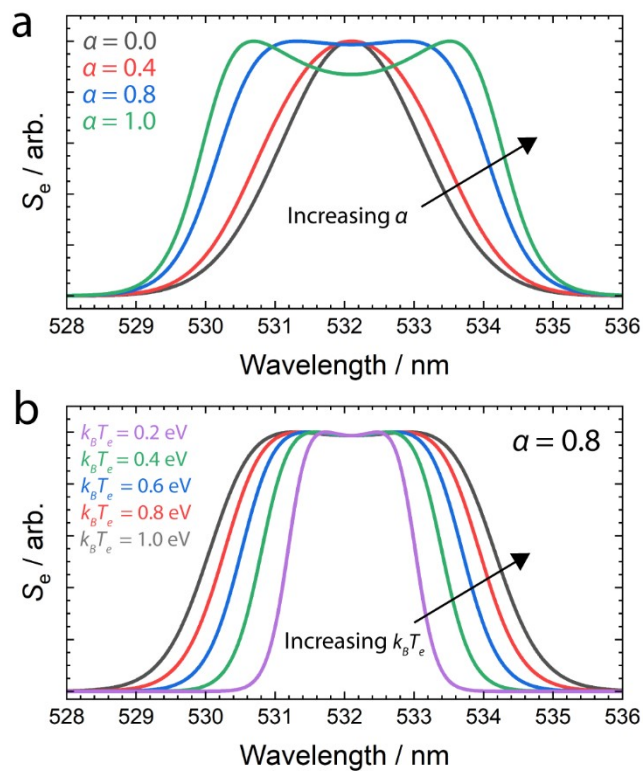


Fig. S4. Effect of scattering parameter and electron temperature on spectral distribution function. (a) The normalized spectral distribution function, S_e , for different values of the scattering parameter, α . (b) The normalized spectral distribution function, S_e , for various electron temperatures, $k_B T_e$, at a constant $\alpha = 0.8$.

Supplementary Note 5: Voltage waveforms of APPJ

The voltage applied to the electrode, V , was estimated based on measuring the peak voltage at powered electrode of the Ar APPJ. More specifically, the voltage waveforms were acquired using a high voltage probe (P6015A, Tektronix) and recorded with a digital oscilloscope (TDS 2014C, Tektronix) for each applied RF power used in the Thomson scattering experiments. Fig. S5 shows the representative voltage waveforms over a single RF cycle. The value of V for a given applied RF power was taken to be the root-mean-square of the peak voltage.

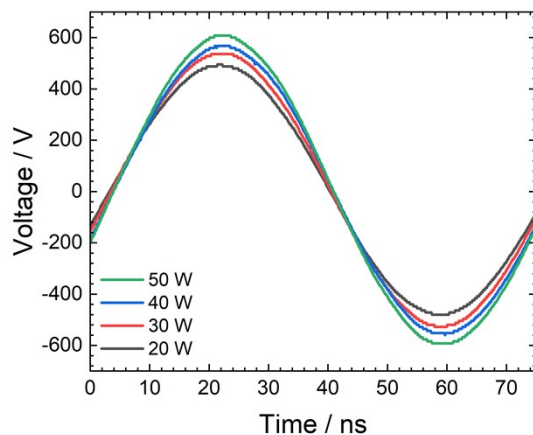


Fig. S5. Voltage waveforms for various applied RF powers. The recorded voltage waveforms over a single RF cycle for the various RF powers used in the Thomson scattering experiments.

Supplementary Note 6: Error Analysis

Error analysis for the floating potential calculations was carried out by propagating the error from the error estimates obtained from the Thomson fitted parameters. The error estimates were outputs along with the fitted parameters from the nlinfit function in Matlab. Specifically, Δn_e and ΔT_e were error estimates for the fitted parameters n_e and T_e , respectively. Propagation of the error estimates from the fitted parameters, the error in the floating potential expression shown in Equation 9 of the main text yields

$$\Delta V_f = \sqrt{\left(-\frac{k_B T_e}{q_e n_e}\right)^2 \Delta n_e^2 + \left[-\frac{2 k_B}{3 q_e} \ln\left(\frac{\mu_+ n_e^{3/2} q_e}{j_+ \sqrt{\frac{k_B T_e}{\epsilon_0}}}\right) - \frac{1 k_B}{3 q_e} - 1.0082 \frac{k_B}{q_e}\right]^2 \Delta T_e^2} \quad (\text{S12})$$

where μ_+ is the ion mobility and j_+ is the ion current density.

Supplementary Note 7: Temporal Variation of Plasma Parameters

The evolution of the plasma parameters (e.g., electron density and electron temperature) determined by laser Thomson scattering was investigated as a function of time and is discussed in detail in an accompanying publication by Yatom et al.⁵ Examples of the n_e and $k_B T_e$ values measured as a function of laser delay time t after the onset of the driving pulse are shown in Fig. S6. The duty cycle was controlled such that the driving pulse controlling the RF power supply was on for a duration of 10 μs , followed by a 40 μs duration in which the RF pulse was turned off. As shown in Fig. S6, the magnitude of both the electron density and electron temperature show an initial spike, followed by a duration where the values remain relatively stable, and an eventual sharp decline as the RF pulse is turned off at $t = 10 \mu\text{s}$. While momentary spikes and/or drops in n_e and $k_B T_e$ were observed, the instantaneous behavior was not found to be representative of the plasma parameters on average. Rather, the time points within the plateau phase (Fig. S6) were designated to represent the average plasma parameters more accurately due to (1) the relatively constant values of n_e and $k_B T_e$ throughout the phase and (2) constituting most of the ‘RF on’ pulse.

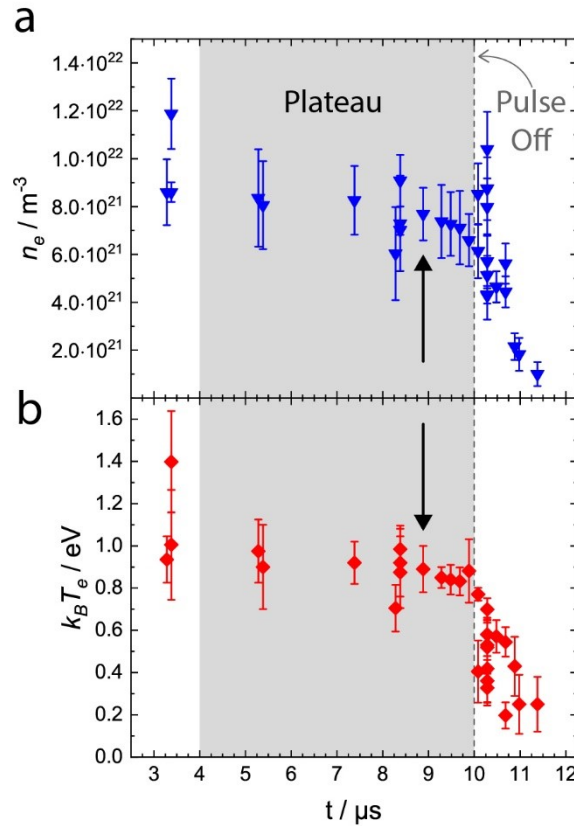


Fig. S6. Plasma parameters as a function of laser delay time. The evolution of (a) electron density and (b) electron temperature as a function of laser delay time holding all other experimental conditions (e.g., argon flow rate, height above liquid, RF power, etc.) constant. Gray shaded area to indicate the plateau phase. Black arrows to illustrate time point corresponding to the Thomson signal shown in Fig. 3b-c in the main text. Dashed line to indicate end of active pulse (i.e., RF is turned off).

Supplementary Note 8: Effect of Concentration on Reduction Potential

To verify the model used for correlating the plasma floating potential to the reduction potential in the liquid, electrochemical measurements were performed in a sodium chloride (NaCl) solution as a function of NaCl concentration using an identical helium APPJ. The electrolyte Debye length, l_D , is related to the NaCl concentration by

$$l_D = \left(\frac{\varepsilon_r \varepsilon_0 k_B T}{N_A q_e^2 \sum_i (c_i \cdot 10^3) z_i^2} \right)^{1/2} \quad (\text{S13})$$

where ε_r is the relative permittivity, T is the temperature of the solution, N_A is the Avogadro constant, c_i is the molar concentration of ionic species i , and z_i is the charge number of ionic species i . According to Equation S13, the value of l_D decreases with increasing electrolyte concentration. Recalling that the model-predicted reduction potential is directly proportional to l_D by

$$\eta = V_f \cdot \frac{l_D}{\lambda_D} \quad (\text{S14})$$

the reduction potential would be expected to decrease for increasing NaCl concentration. Measurements of the relative reduction potential were measured for NaCl solutions with nominal concentrations of 0.2, 2, 20, and 200 mM. Solutions were freshly prepared using Type III ultrapure (18.2 MΩ cm) water from a Direct-Q 3 Water Purification System (MilliporeSigma). The plasma source used the same powered nickel needle electrode, but the tube used in this experiment was a fused silica tube with inner and outer diameters of 7 mm and 9.5 mm, respectively. The ground electrode was an aluminum ring with an inner diameter of 9.5 mm, which was mounted to the exterior of the silica tube at a distance of 5 mm from the tube outlet. The operating gas was helium, which was maintained at a constant flow rate of 2000 sccm. The RF power supply was run in continuous mode rather than a pulsed mode, using an applied RF power of 50 W. Electrochemical characterization was performed using a Ag/AgCl reference electrode to measure the local potential within the liquid directly underneath the plasma-liquid interface, E_{PLI} , relative to the potential measured by a nominally identical Ag/AgCl reference electrode positioned far away in the bulk NaCl solution, E_{inf} . The reference electrode measuring E_{PLI} was housed in a Luggin capillary, allowing it to be positioned in the solution immediately underneath the impingement point of the plasma jet without physically perturbing the plasma. A schematic of the experimental apparatus is shown in Fig. S7a.

The floating potential was calculated using the same collision-dominated model^{6,7} described in the main text, given by

$$V_f = -\frac{2}{3} \frac{k_B T_e}{q_e} \ln \frac{\Delta}{\lambda_D} - 1.0082 \frac{k_B T_e}{q_e} \quad (\text{S15})$$

where Δ is the ionization length. The ionization length can be written as

$$\Delta = \frac{n_e k_B T_e \mu_+}{j_+} \quad (\text{S16})$$

where the ion current density can be approximated using the Child-Langmuir law given by⁸

$$j_+ = \frac{4}{9} \varepsilon_0 \left(\frac{2q_e}{M_+} \right) V^{3/2} \quad (\text{S17})$$

where M_+ is the ion mass and d is the interelectrode spacing. The ionic species dependence in the floating potential calculation arise from the M_+ and μ_+ terms which are $6.64 \cdot 10^{-27}$ kg and $10.7 \cdot 10^{-4}$ m² V⁻¹ s⁻¹, respectively, in the case of helium.^{9,10} Given that the helium APPJ was not characterized, the plasma parameters were set to be $n_e = 1 \cdot 10^{21}$ m⁻³ and $k_B T_e = 2.0$ eV for the floating potential calculation. In general,

work comparing RF atmospheric helium and argon plasmas report lower electron densities and higher electron densities for the helium plasmas under similar operating conditions.¹¹ Based on the electron temperatures and electron densities obtained for the Ar APPJ from the Thomson scattering experiments, these estimates for the He APPJ plasma parameters are within reason. A plot of the model-predicted reduction values and the experimentally measured values for the reduction potential as a function of NaCl concentration are shown in Fig. S7b.

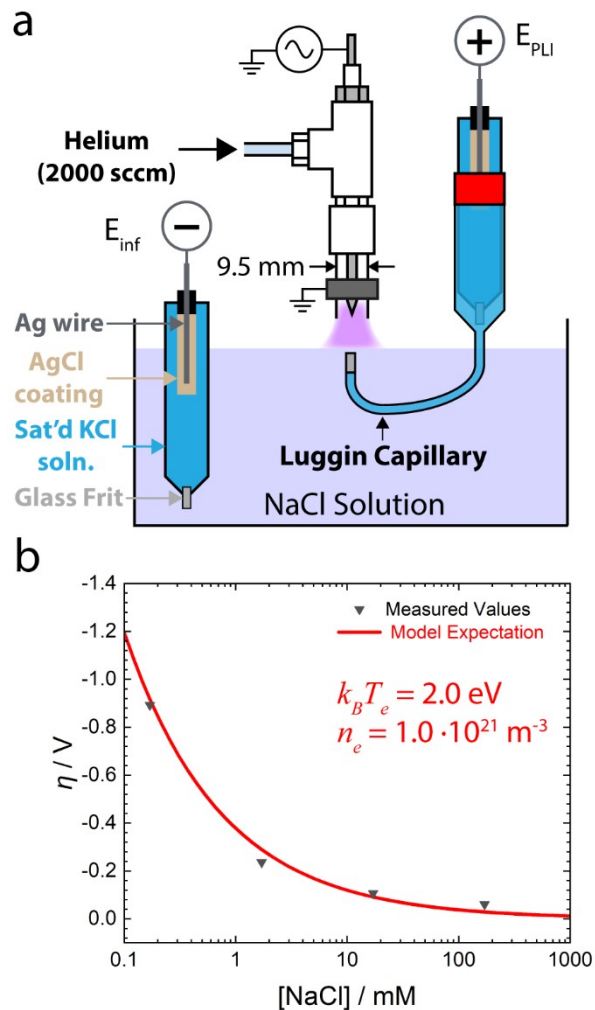


Fig. S7. Effect of electrolyte Debye length on reduction potential. (a) Schematic representation helium APPJ and reference electrode, E_{PLI} , housed in a Luggin capillary used to measure local potential in the liquid near the plasma-liquid interface with respect to an identical reference electrode fixed in the bulk NaCl solution, E_{inf} . (b) The experimentally measured reduction potential (black triangles) for a helium APPJ in contact with a NaCl solution and the model-predicted reduction potential (red line) as a function of NaCl concentration. The plasma parameters assumed for the floating potential calculation were $k_B T_e = 2.0$ eV and $n_e = 1 \cdot 10^{21} \text{ m}^{-3}$ as indicated.

References

- 1 T. P. Hughes, *Plasmas and laser light*, Wiley, New York, 1975.
- 2 S. Bivona, R. Daniele and G. Ferrante, Laser-assisted inverse bremsstrahlung in a weakly ionised plasma, *J. Phys. B: Atom. Mol. Phys.*, 1982, **15**, 1585–1599.
- 3 E. A. D. Carbone, J. M. Palomares, S. Hübner, E. Iordanova and J. J. A. M. van der Mullen, Revision of the criterion to avoid electron heating during laser aided plasma diagnostics (LAPD), *J. Inst.*, 2012, **7**, C01016–C01016.
- 4 T. Oldham, M. Chen, S. Sharkey, K. M. Parker and E. Thimsen, Electrochemical characterization of the plasma-water interface, *J. Phys. D: Appl. Phys.*, 2020, **53**, 165202.
- 5 S. Yatom, T. Oldham and E. Thimsen, Characterization of plasma in RF jet interacting with water: Thomson scattering versus Spectral line broadening, *Plasma Sources Sci. Technol.*, 2022, Submitted.
- 6 M. S. Benilov and S. Coulombe, Modeling a collision-dominated space-charge sheath in high-pressure arc discharges, *Physics of Plasmas*, 2001, **8**, 4227–4233.
- 7 M. S. Benilov, The Child–Langmuir law and analytical theory of collisionless to collision-dominated sheaths, *Plasma Sources Sci. Technol.*, 2009, **18**, 014005.
- 8 I. Langmuir, The Effect of Space Charge and Residual Gases on Thermionic Currents in High Vacuum, *Phys. Rev.*, 1913, **2**, 450–486.
- 9 H. J. Oskam and V. R. Mittelstadt, Ion Mobilities in Helium, Neon, and Argon, *Phys. Rev.*, 1963, **132**, 1435–1444.
- 10 K. Jousten, Ed., *Handbuch Vakuumtechnik*, Springer Vieweg, Wiesbaden [Heidelberg], 12., neu bearbeitete Auflage., 2018.
- 11 S.-Z. Li, J.-P. Lim, J. G. Kang and H. S. Uhm, Comparison of atmospheric-pressure helium and argon plasmas generated by capacitively coupled radio-frequency discharge, *Physics of Plasmas*, 2006, **13**, 093503.